

ATOMISTIC SIMULATION STUDY OF INDENTATION OF METALLIC NANOWIRES

A Thesis
Presented to the Faculty of the
College of Engineering and Mathematical Sciences
and Honors College of the
University of Vermont
in Partial Fulfillment of the Requirements for the Graduation of the
Honors College

by
Trevor Avant
April 2011

ACKNOWLEDGEMENTS

First I would like to thank my advisor Prof. Frederic Sansoz. He has been extremely helpful from the start. He gave me all the tools I needed, so that I could be as successful as my effort allowed me. I especially thank him for finding support for allowing me to work in the lab over the summer. That was a pivotal experience in both my research and my academic career.

I also thank all members of the Sansoz Lab. I thank Jessie Gu for all things simulation. I thank Erin Wood for all things experimental. And I thank Evan Malina for all things fantasy baseball and skiing.

ABSTRACT

The mechanical properties of metallic nanowires, such as hardness and tensile strength, are of fundamental importance in the field of nanotechnology. In this thesis, molecular dynamics simulations were used to fundamentally understand the process of nanoindentation in cylindrical metallic nanowires less than 30 nm in diameter, and to characterize the effects of crystal orientation and metal type on hardness measurements in this type of nanowires. All simulated nanowires were face-centered cubic single-crystals in nickel and gold with $\langle 111 \rangle$ axis and a circular cross-section. Different models involved wires oriented at different angles with respect to the tip position. An analysis of deformation mechanisms at the atomic scale was performed using the atomistic simulation software LAMMPS. A more quantitative analysis was also performed using equations derived from classical mechanics. The elastic modulus, maximum pressure at yield point, and hardness obtained by the nanoindentation simulations were analyzed in detail. Simulation results show that different angles of the nanowire do result in different properties, which can be related back to the nucleation and emission process of prismatic loops under the penetrating tip.

Contents

| | |
|---|-----|
| ACKNOWLEDGEMENTS..... | ii |
| ABSTRACT..... | iii |
| CHAPTER 1: INTRODUCTION | 2 |
| 1.1 Background and Justification | 2 |
| 1.2 Objectives..... | 2 |
| CHAPTER 2: EXPERIMENTAL METHODS | 3 |
| 2.1 Simulations..... | 3 |
| 2.2 Calculations..... | 4 |
| 2.2.1 Rotation Angles..... | 4 |
| 2.2.2 Ackland Numbers | 5 |
| 2.2.3 Mean Contact Pressure..... | 5 |
| 2.2.3 Hardness | 5 |
| 2.2.4 Maximum Pressure | 5 |
| 2.2.5 Young's Modulus..... | 5 |
| CHAPTER 3: RESULTS..... | 7 |
| 3.1 0° Model..... | 7 |
| 3.2 10.893° Model..... | 10 |
| 3.3 30° Model..... | 12 |
| 3.4 49.107° Model & 60° Model | 14 |
| 3.5 Young's Modulus..... | 16 |
| 3.6 Hardness & Max Pressure | 17 |
| CHAPTER 4: INTERPRETATION OF RESULTS | 18 |
| 4.1 Inconsistencies in the 30° Model | 18 |
| 4.2 Separation of the Nucleation and Emission Stages | 18 |
| 4.3 Young's Modulus, Max Pressure and Hardness as a Function of Angle | 18 |
| CHAPTER 5: SUMMARY, CONCLUSIONS & FUTURE WORK..... | 20 |
| 5.1 Summary | 20 |
| 5.2 Conclusions& Future Work | 20 |
| REFERENCES..... | 21 |
| APPENDIX..... | 22 |

CHAPTER 1: INTRODUCTION

1.1 Background and Justification

Nanotechnology is one of the most promising and exciting fields being researched today. It investigates structures and materials which are on the scale of less than 100 nanometers. Nanomaterials are the building blocks of nanotechnology. Studying materials on such a small scale is significantly different from studying materials on the macro and micro scale. Materials science had typically relied upon examining properties based on microstructures, such as grain size. Nanomaterials must be regarded as an arrangement of atoms. Research into the field of nanomaterials has led to groundbreaking findings. As materials get smaller, their properties begin to change. Prior to the study of nanomaterials, materials were generally thought of as having properties that are scale-independent. Now, scientists and engineers are beginning to learn that as nanomaterials get smaller, they get softer or even stronger.

Metal nanowires are fundamental structures in the field of nanomaterials. Their wide-ranging applications give promise to advances in biology, photonics, and electromechanics [1-4]. One of an engineer's biggest concerns is the way in which they deform under an external force. Indentation tests and compression tests are two of the most useful methods for studying a material's resistance to deformation. However, attempting to perform these tests on wires only several nanometers in diameter raises technical challenges. No one has yet been able to perform a compression test on a nanowire at such a small scale. Instead, more performable experiments such as nanoindentation tests have been implemented. Nanoindentation tests have been successfully performed with the use of atomic force microscopy. The Sansoz Lab at UVM has performed many simulation-based studies of metallic nanowires [5-8].

Although atomic force microscopy is a very useful experimental tool, it does not allow us to fully understand what is occurring at the molecular scale. Molecular dynamics (MD) simulations are a solution to this problem. Originally developed by physicists, molecular dynamics simulations have become profoundly useful in the field of materials science. These simulations, which rely upon a massive amount of computational resources, were not possible before the age of high-performance computing. Today, MD simulations are sophisticated enough to model nanoindentation with a high degree of accuracy. They have proven to be an invaluable resource in the visualization and calculation of atomic responses to force.

1.2 Objectives

- Use molecular dynamics simulations to simulate the indentation of [1 1 1]-oriented nickel
- Model different rotations of nanowires (all still having a [1 1 1] orientation)
- Calculate and characterize the differences in hardness of the nanowires, due to the effect of rotation

CHAPTER 2: EXPERIMENTAL METHODS

2.1 Simulations

The molecular dynamics software which was used was developed at Sandia National Laboratory and is called LAMMPS (Large-scale Atomic/Molecular Massively Parallel Simulator).

Five different face-centered cubic (FCC), nickel nanowires were modeled. All five models were identical except for the crystal orientation. The orientation along the axis of the wire (x-direction) was the same for all wires ([1 1 1]), but the orientation in the other two directions (y and z-directions) was changed. This effectively simulated the wire being rotated about its axis. The angles of rotation were calculated for each model, and are shown in Table 2.1.

All five models were 30 nm in diameter and 40 nm in length. Periodic boundary conditions were applied along the direction of the wire axis, and fixed in the other two directions. The bottom two atomic layers were constrained by zeroing both their force and velocity in all directions. This was done to prevent the wire from moving during indentation. The embedded-atom method (EAM) was used as the interatomic potential for all atoms. The data for the EAM potentials which was used is given by Mishin et al. [9]. A virtual, spherical indenter was used to simulate indentation. The indenter had a radius of 8.91 nm. The surface of the sphere was positioned at an original distance of 0.2 nm from the surface of the wire. It was moved toward the wire at a rate of 1 m/s. The force the indenter exerted on each atom was determined by the formula

$$F(r) = -k(r - R)^2 \quad (2.1)$$

where k is a force constant of 10 N/m^2 , r is the distance from an atom to the center of the indenter, and R is the radius of the indenter. A diagram of the wire and indenter are shown in Figure 2.1.

Before any indentation was implemented, the nanowires were subjected to an energy minimization process. The conjugate gradient (CG) algorithm was used to "relax" the wire. For the indentation process, the temperature of each simulation was set at 300 K and was implemented through a Nose/Hoover NVT time integration. Each timestep was 5 fs and simulations were run for 400,000 timesteps. Thus each full simulation was 2 ns long. So, by the end of a simulation, the indenter had moved a total of 1.8 nm into the surface of the wire. The coordinates, Ackland number (discussed in Section 2.2.2), identification number, and atom type were output every 2,500 timesteps.

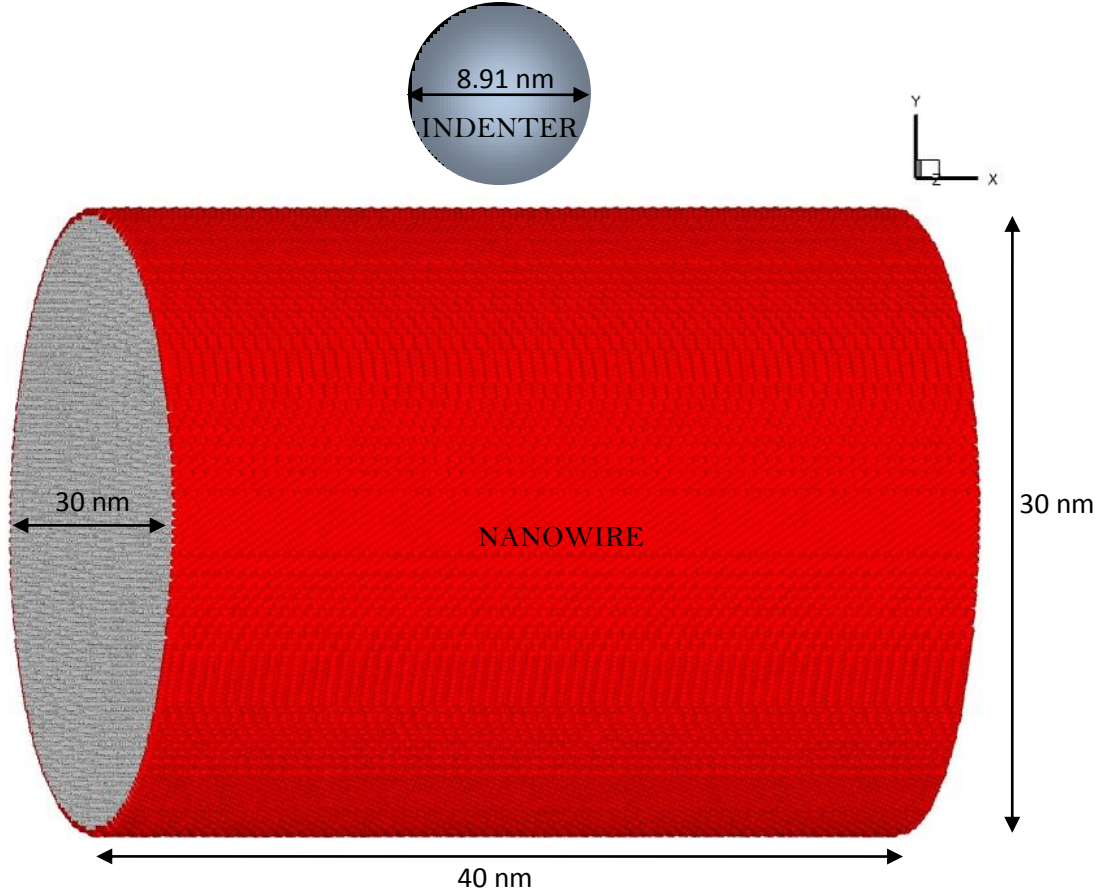


Figure 2.1. Dimensions of the nanowire model and the spherical indenter for all five models.

2.2 Calculations

2.2.1 Rotation Angles

All five nanowires were oriented with the axis running along the $[1\ 1\ 1]$ crystal direction (the x-direction in the simulation). The crystal orientation along the simulation's y and z axes were altered to produce different angles of rotation. The angle which was chosen to represent 0° was oriented in the $[1\ 1\ \bar{2}]$ direction on the y-axis and the $[\bar{1}\ 1\ 0]$ direction on the x-axis. Four other orientations along the x and y-axes were chosen which would create wires which were rotated from the 0° position. The angle of rotation from the 0° position was calculated using the formula:

$$\cos \theta = \frac{a \cdot b}{\|a\| \|b\|} \quad (2.2)$$

The five angles and orientations in the x, y and z-directions of the models are shown in Table 2.1.

| x-Axis Orientation | y-Axis Orientation | z-Axis Orientation | Angle |
|--------------------|---------------------------|--------------------|---------|
| [1 1 1] | [1 1 $\bar{2}$] | [$\bar{1}$ 1 0] | 0° |
| [1 1 1] | [1 2 $\bar{3}$] | [$\bar{5}$ 4 1] | 10.893° |
| [1 1 1] | [0 1 $\bar{1}$] | [$\bar{2}$ 1 1] | 30° |
| [1 1 1] | [$\bar{1}$ 3 $\bar{2}$] | [$\bar{5}$ 1 4] | 49.107° |
| [1 1 1] | [$\bar{1}$ 2 $\bar{1}$] | [1 0 $\bar{1}$] | 60° |

Table 2.1: Crystal directions and resulting angles for the five models.

2.2.2 Ackland Numbers

In order to help in the visualization process, LAMMPS was used to determine the Ackland number of each atom. The Ackland number represents the local lattice structure of each atom and is given in Ackland et al. [10]. All cross-sectional images shown in this thesis use the Ackland number to hide all FCC atoms.

2.2.3 Mean Contact Pressure

The mean contact pressure, p_m , from the indenter is a property which is used to help determine hardness. It was determined using the formula:

$$p_m = \frac{P}{A} \quad (2.3)$$

where P is the total force applied to all of the atoms and A is the projected contact area. The contact area A was calculated using formulation determined by Feng et al. [11].

2.2.3 Hardness

In order to calculate hardness, values for mean contact pressure beyond the elastic regime were averaged. To be consistent among all models, all mean contact pressure data points with a penetration depth greater than 1.0 nm were averaged.

2.2.4 Maximum Pressure

The maximum pressure was also used as an indicator of hardness. This value was simply the highest value the mean contact pressure reached. It occurred prior to the first dislocation for all of the wires.

2.2.5 Young's Modulus

The Young's modulus was also calculated using the Hertz theory [12]. The theory determines contact load using the formula:

$$P = \frac{4}{3} \sqrt{R \frac{E}{1 - \nu^2}} \delta^{3/2} \quad (2.4)$$

where δ is the penetration depth, ν is the Poisson's ratio ($\nu = 0.312$ for nickel [13]), and E is Young's modulus. The term R is a function of the indenter radius R_i and the wire radius R_f , which are expressed as:

$$\frac{1}{R} = \frac{1}{R_i} + \frac{1}{R_f} \quad (2.5)$$

Throughout indentation, R , E , and ν were taken as constants, which reduces Eq. 2.4 to:

$$P = C\delta^{3/2} \quad (2.6)$$

The force-displacement curve output by the MD simulation, was fitted with Eq. 2.6 to determine C . The curve was fitted from the origin to the yield point. Based on the value of C , the Young's modulus was solved for as:

$$E = \frac{3(1 - \nu^2)}{4\sqrt{R}} C \quad (2.7)$$

CHAPTER 3: RESULTS

3.1 0° Model

Contact force and penetration depth are graphed in Figure 3.1.

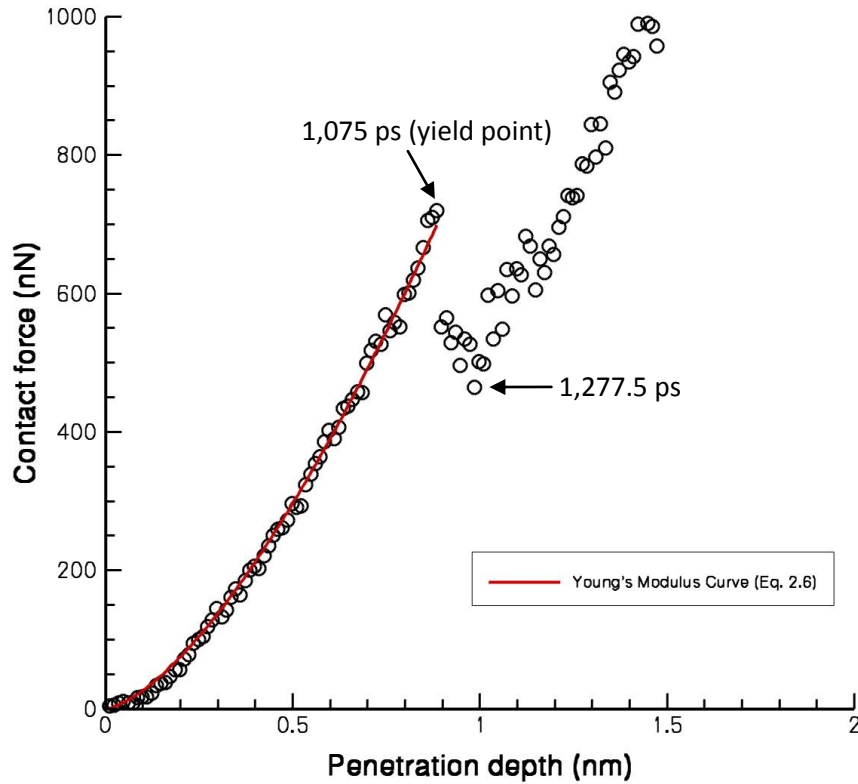


Figure 3.1. Contact force v. penetration depth for the simulation of the 0° nanowire. From the curve and Eq. 2.7, Young's modulus was calculated to be 240.0 GPa. Arrows indicate notable points in the dislocation process.

The yield point and of the elastic regime very clearly occurs at 1,075 ps. This corresponds to the nucleation of the first dislocation loops in the model. Eq. 2.6 was fitted to all points in the elastic regime. The curve fit the data quite well. The resulting C value was then used in Eq. 2.7 to calculate a Young's modulus of 240.0 GPa. Mean contact pressure was also compared to penetration depth, and is graphed in Figure 3.2.

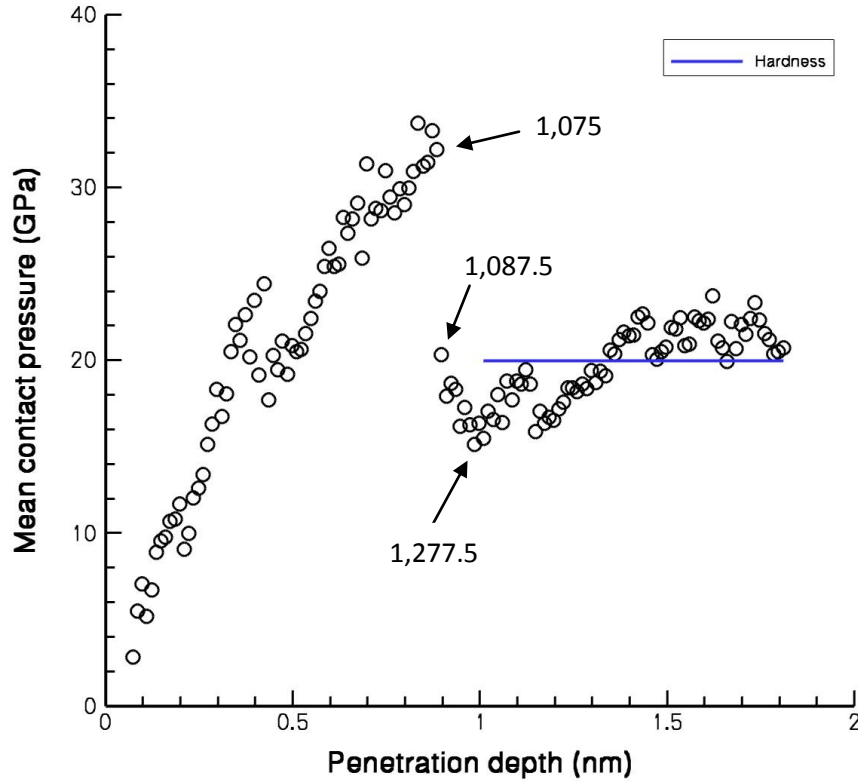


Figure 3.2. Mean contact pressure v. penetration depth for the simulation of the 0° nanowire. Hardness was calculated at 20.0 GPa.

The hardness was calculated to be 20.0 GPa. Both the force and pressure increase until 1,075 ps. After that, force and pressure both decrease, which corresponds to the nucleation of the first prismatic dislocation loop (Figure 3.4). Force and pressure continue to decrease as the loop continues to nucleate. Shortly after nucleation has occurred, the prismatic loop is emitted from the indentation zone and absorbed by the free surface of the wire (Figure 3.5).

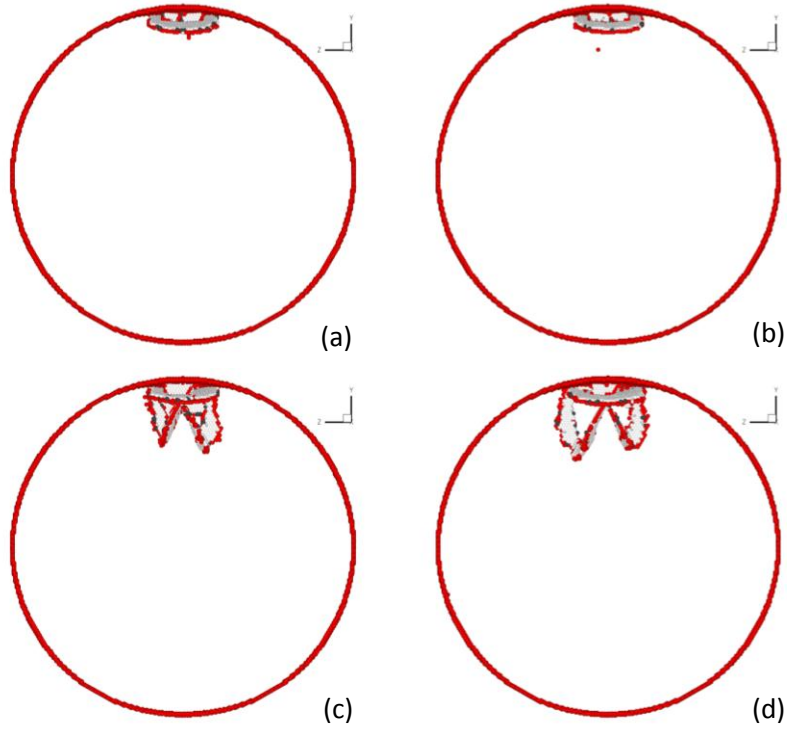


Figure 3.4. Nucleation of a loop in the 0° nanowire at (a) 1,062.5 ps, (b) 1,075 ps, (c) 1,087.5 ps and (d) 1,100 ps. Note all FCC atoms are hidden to show the loops.

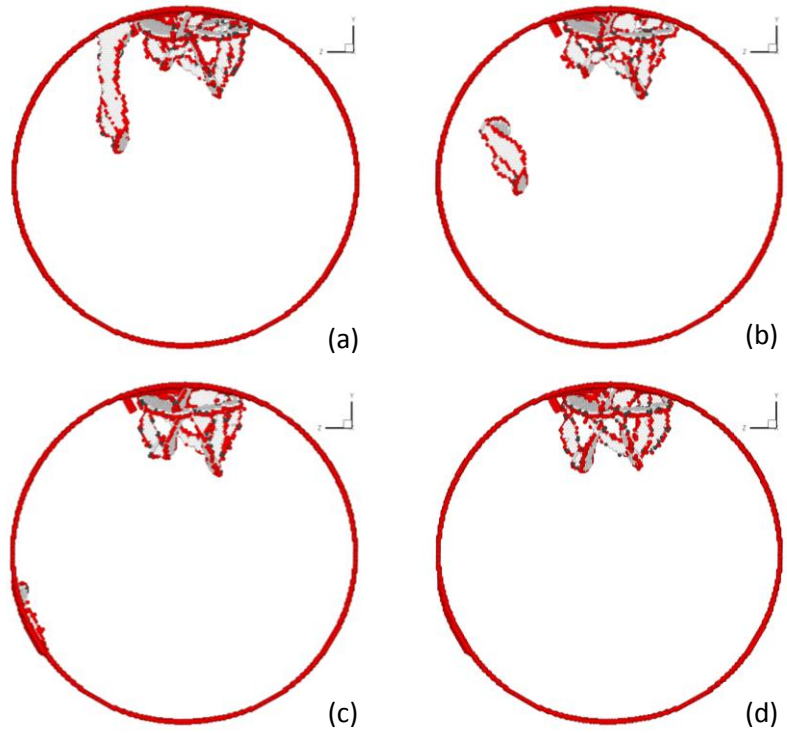


Figure 3.5. Evolution of a prismatic loop in the 0° nanowire, shown in increments of 5 ps. (a) A dislocation loop forming at the top of the wire, (b) moving through the body of the wire, (c) being absorbed by the free surface and (d) fully absorbed into the free surface.

3.2 10.893° Model

The force-penetration depth curve is shown in Figure 3.6, while the mean contact pressure-penetration depth curve is shown in Figure 3.7.

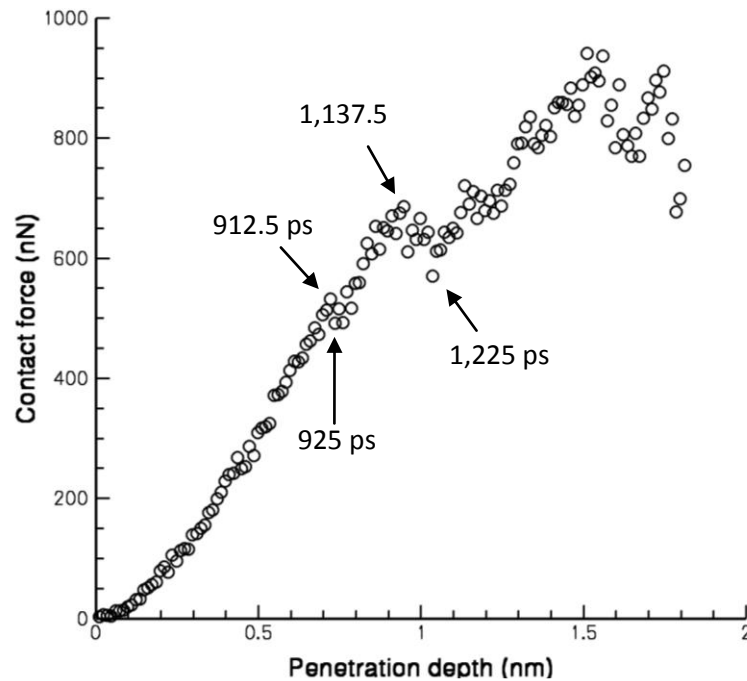


Figure 3.6. Contact force v. penetration depth for the simulation of the 10.893° nanowire.

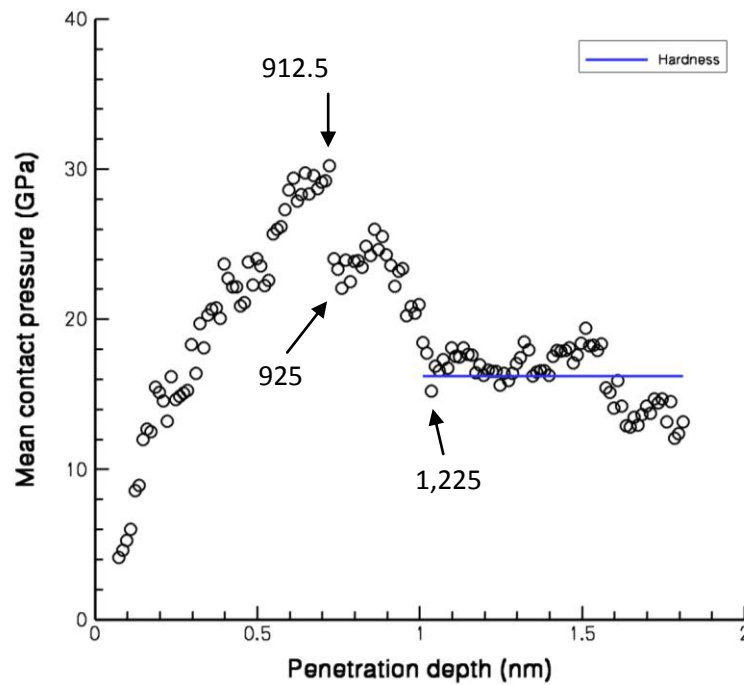


Figure 3.7. Mean contact pressure v. penetration depth for the simulation of the 10.893° nanowire. Hardness was calculated to be 16.2 GPa.

The yield point of the force-penetration depth curve (Figure 3.6) does not occur as clearly as in the 0° nanowire (Figure 3.1). At 912.5 ps there is a small decrease in force, followed by a larger one at 1,137.5 ps. After analyzing images of the wire during simulation, it can be determined that the nucleation of the first loops occurs around 912.5 ps (Figure 3.9) and the emission of that loop occurs around 1,225 ps. The dynamics which produce this behavior are illustrated in Figure 3.9 and Figure 3.10. Eq. 2.6 was fit to the penetration depth-contact force curve up until the first nucleation (at 912.5 ps). These results are shown in Figure 3.11.

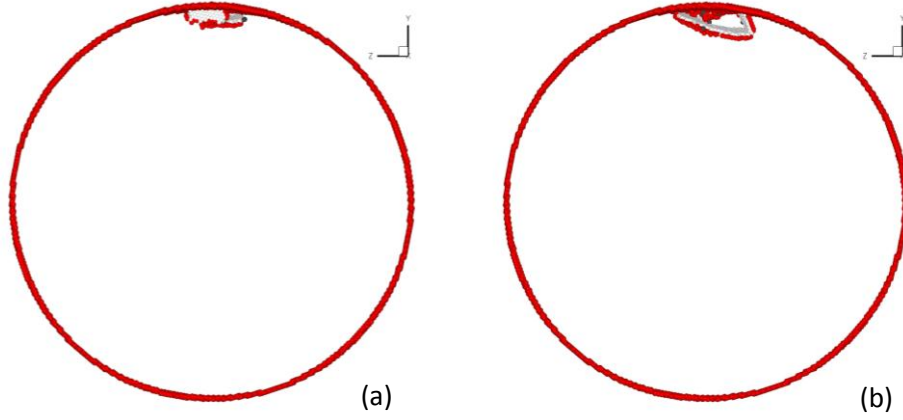


Figure 3.9. Nucleation of a loop shown at 912.5 ps (a) and 925 ps (b).

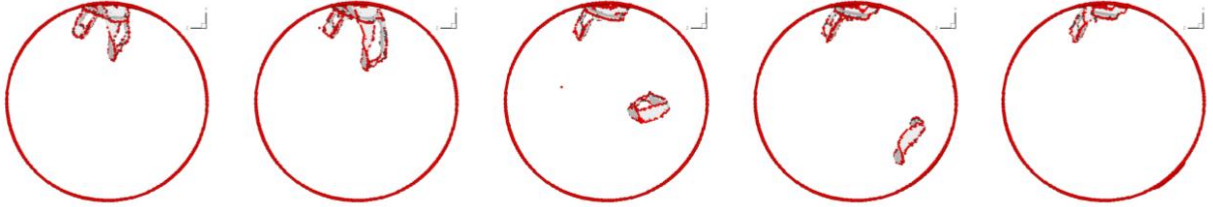


Figure 3.10. Left to right, emission of a prismatic loop from 1,200 ps to 1,250 ps. In increments of 12.5 ps.

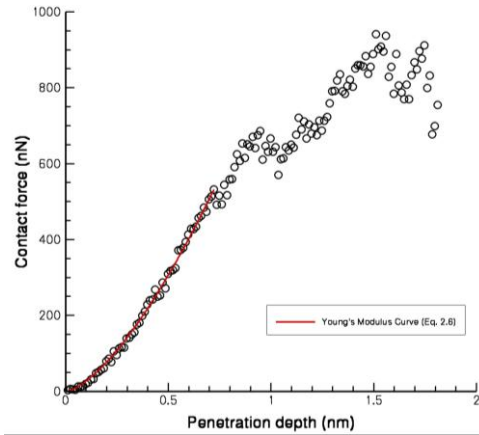


Figure 3.11. Contact force v. penetration depth for the simulation of the 10.893° nanowire. From the curve and Eq. 2.7, Young's modulus was calculated to be 240.0 GPa.

3.3 30° Model

Force and penetration depth curve are shown in Figure 3.12.

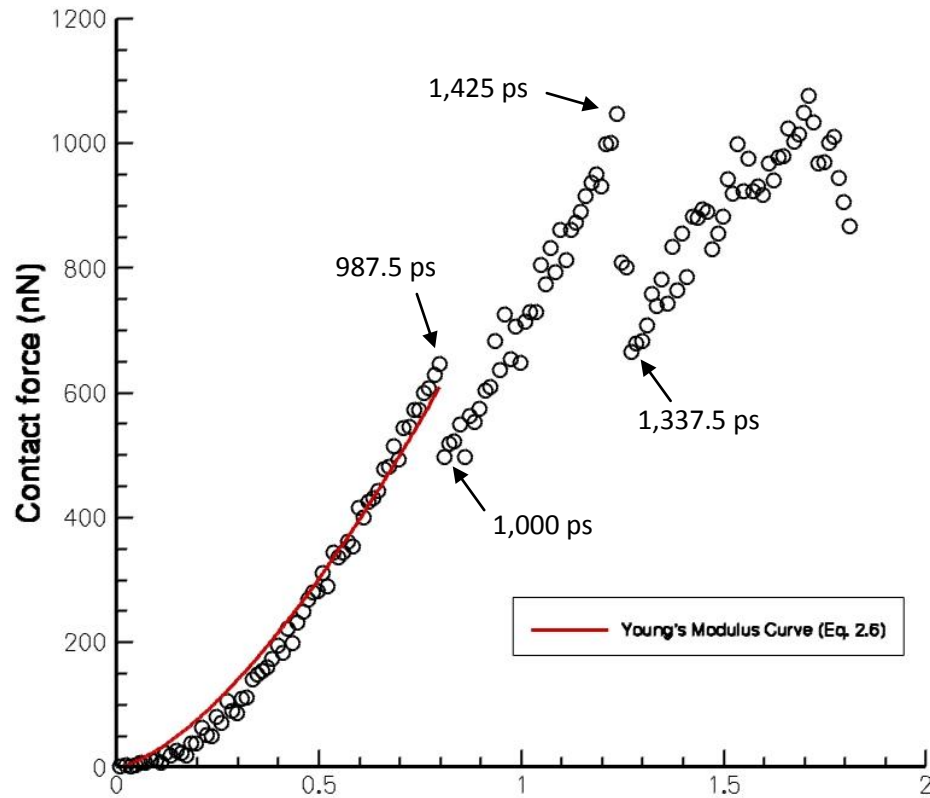


Figure 3.12. Contact force v. penetration depth for the simulation of the 30° nanowire. From the curve and Eq. 2.7, Young's modulus was calculated to be 244.2 GPa.

Eq. 2.6, which was used to calculate Young's modulus, did not fit the data as well as it did for the 0° and 10.893° models. The chi-square fit for this value was calculated to be 44,371, which was over four times larger than the largest chi-square value of all other models (all chi-square fit values are shown in Table A.4). Young's modulus was calculated to be 244.2 GPa. Mean contact pressure is shown in Figure 3.13.

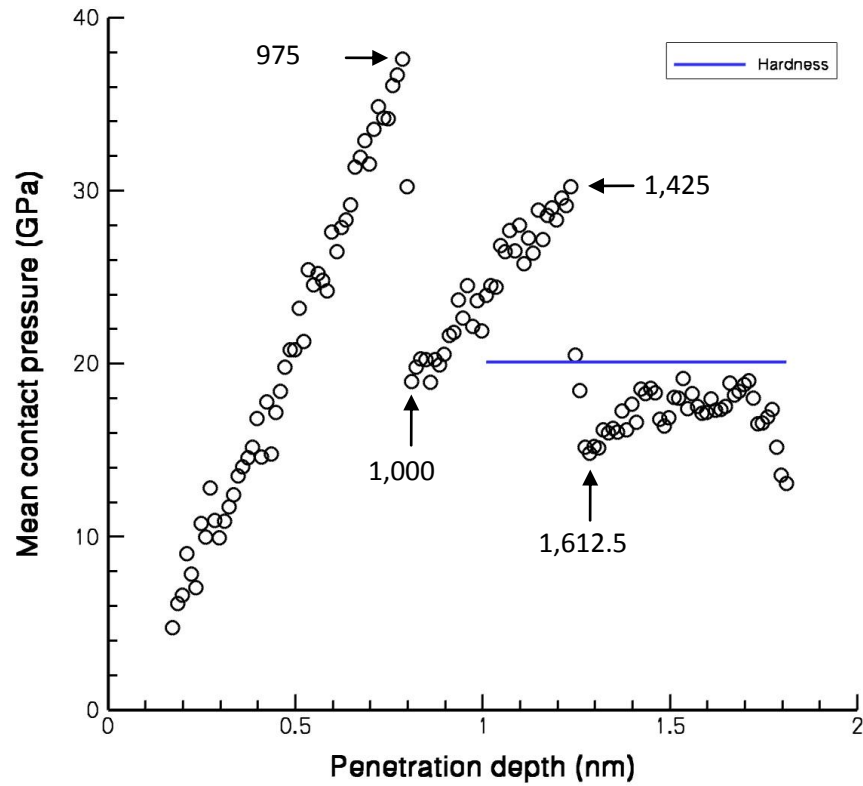


Figure 3.13. Mean contact pressure v. penetration depth for the simulation of the 30° nanowire. Hardness was calculated to be 20.1 GPa.

Similar to the 10.893° model, the dislocation/emission process occurs in two stages. In the first stage, between 975 ps and 1,000 ps, the loop nucleates (Figure 3.14). In the second stage, between 1,425 ps and 1,612.5 ps, the loop is emitted into the center of the wire (Figure 3.15).

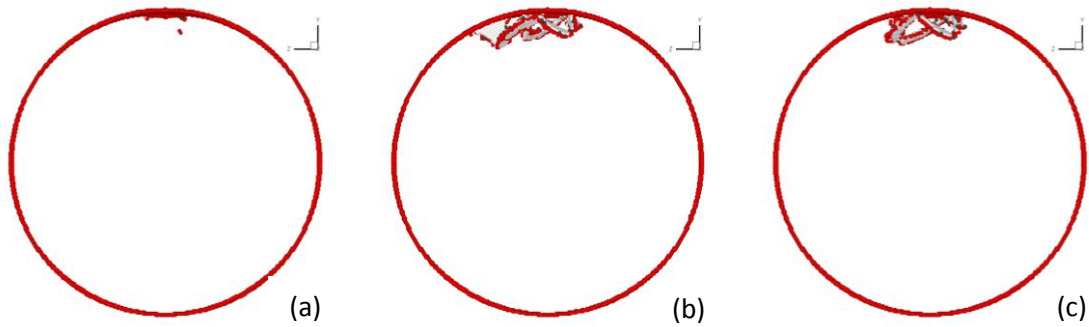


Figure 3.14. Nucleation of a dislocation loop shown at (a) 975 ps, (b) 987.5 ps and (c) 1,000 ps.

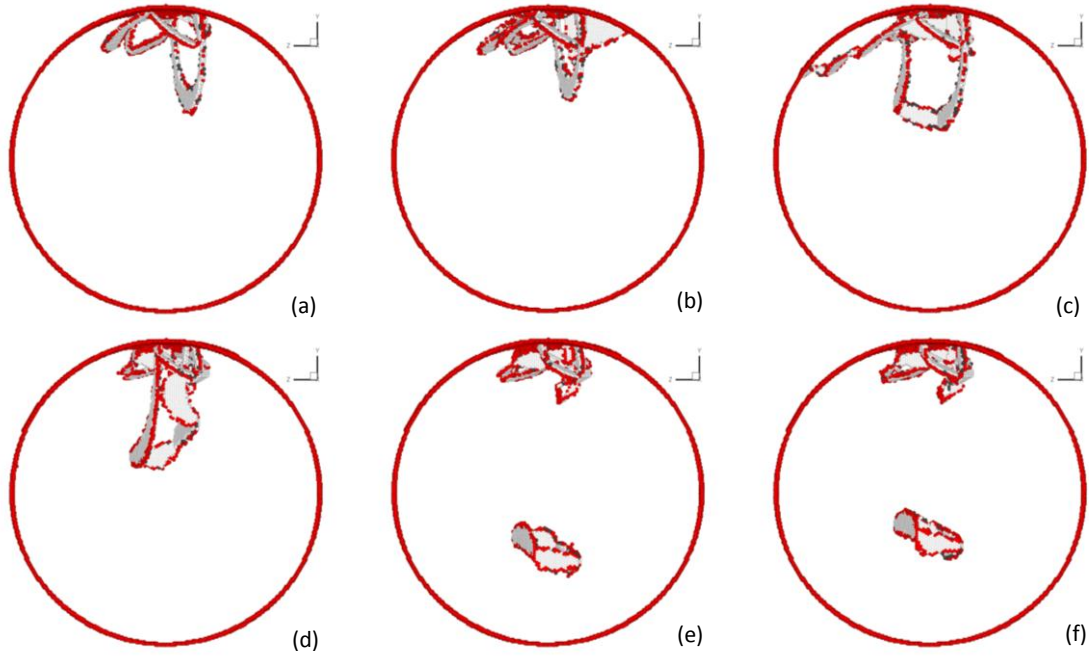


Figure 3.15. Prismatic loop being emitted from the 30° nanowire. (a) 1,425 ps, (b) 1,437.5 ps, (c) 1,450ps, (d) 1,462.5 ps, (e) 1,475 ps and (f) 1,487.5 ps.

Figure 3.15 shows a peculiar behavior of the dislocation loop. It remains inside of the wire and is not absorbed by the free surface. It remains inside of the wire for the rest of the simulation. Explanations for this behavior are discussed in Section 4.1.

3.4 49.107° Model & 60° Model

The 49.107° and 60° were the final two models to be simulated. The dynamics of these simulations consist of the nucleation of prismatic loops, emission of the loops through the wire, and absorption into the free surfaces of the nanowire. These processes are very similar to those shown for previous wires, and are not shown in detail. The contact force and mean contact pressure are shown in Figure 3.16 for the 49.107° nanowire and in Figure 3.17 for the 60° nanowire.

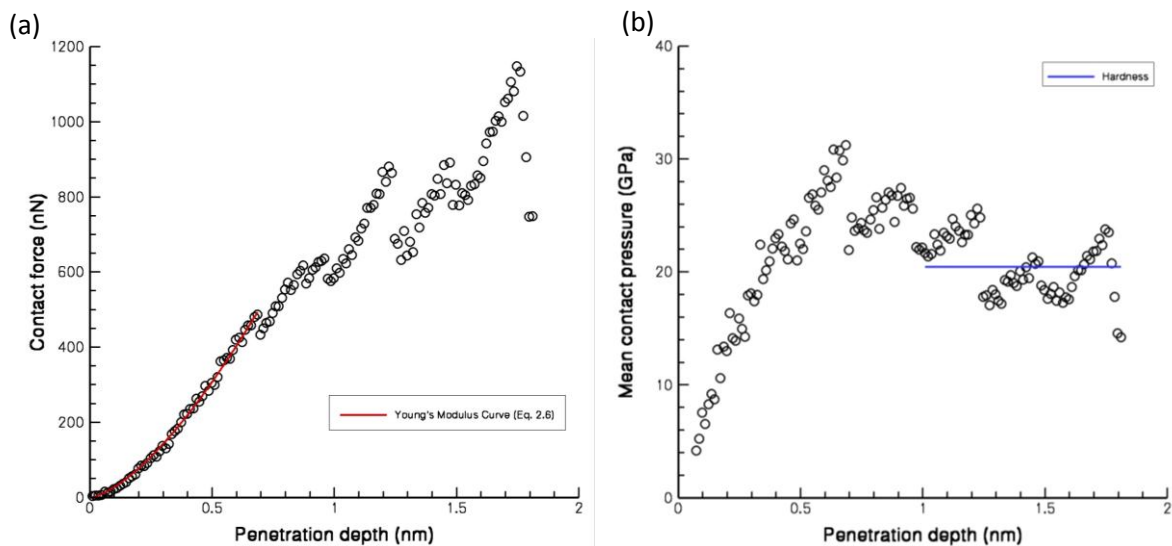


Figure 3.16. Properties of the 49.107° nanowire. (a) Contact force v. penetration depth. From the curve and Eq. 2.7, Young's modulus was calculated to be 248.5 GPa. (b) Mean contact pressure v. penetration depth. Hardness was calculated to be 19.746 GPa.

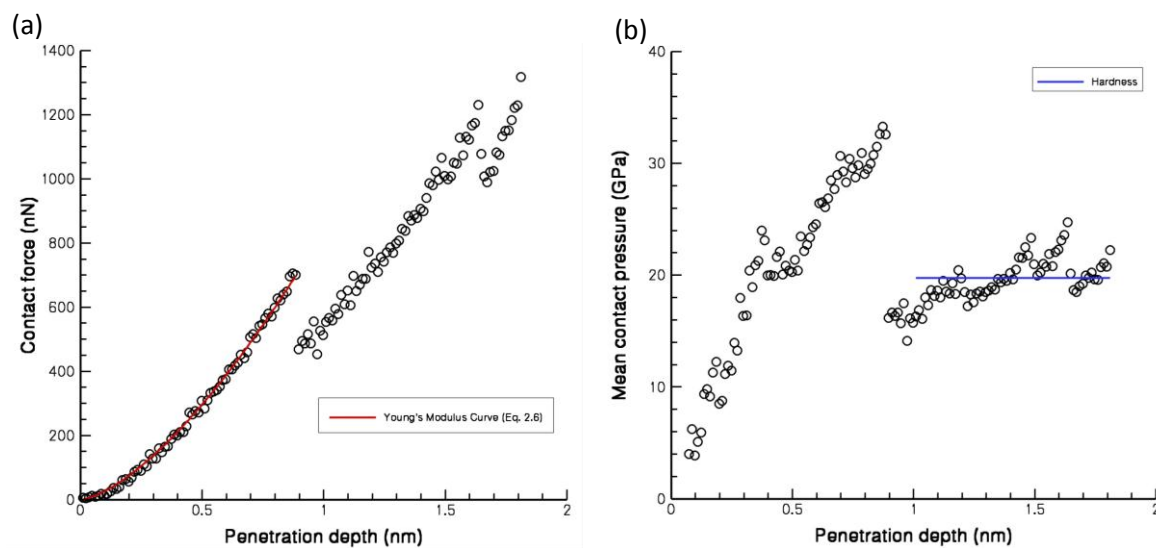


Figure 3.17. Properties of the 60° nanowire. (a) Contact force v. penetration depth. From the curve and Eq. 2.7, Young's modulus was calculated to be 239.6 GPa. (b) Mean contact pressure v. penetration depth. Hardness was calculated to be 20.5 GPa.

3.5 Young's Modulus

The Young's modulus values for all five simulations are graphed together in Figure 3.18. These values are also shown together in Table 3.1.

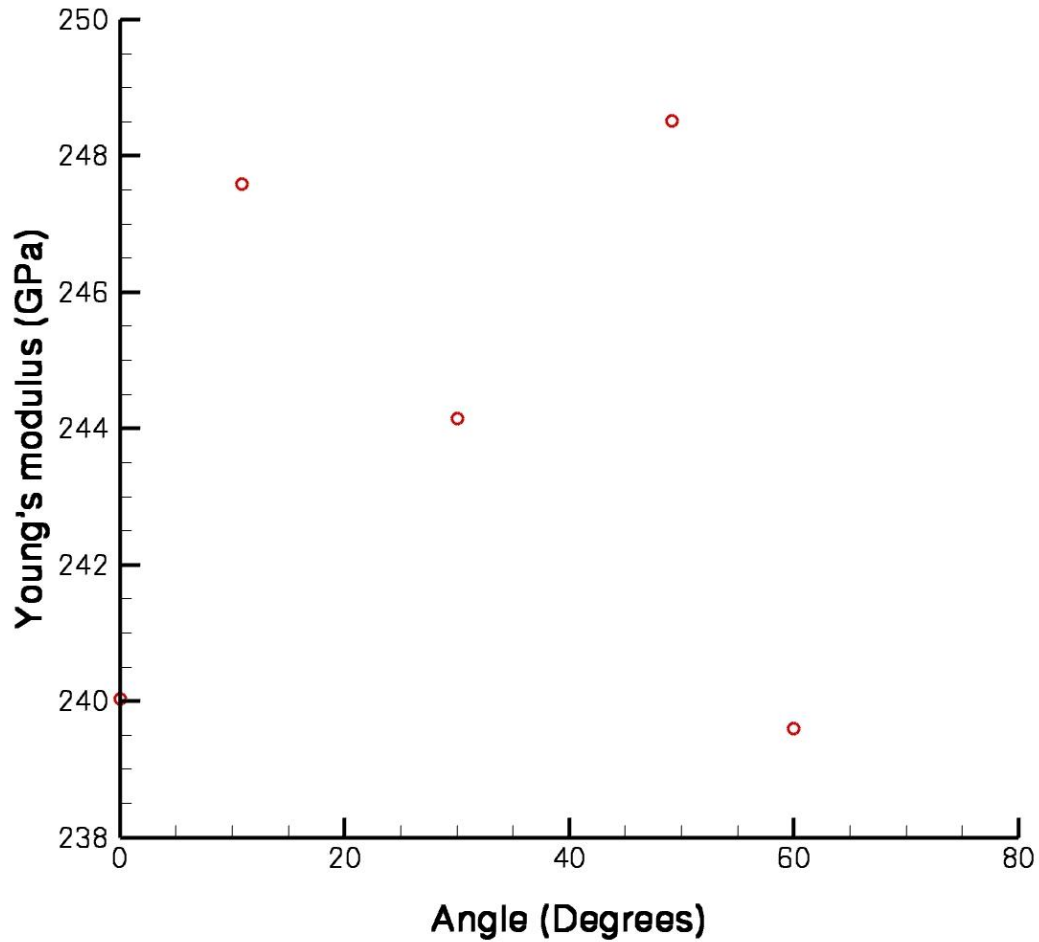


Figure 3.18. Young's modulus for each of the five simulations.

3.6 Hardness & Max Pressure

Hardness and max pressure are graphed together in Figure 3.19. Additionally, they are shown in Table 3.1.

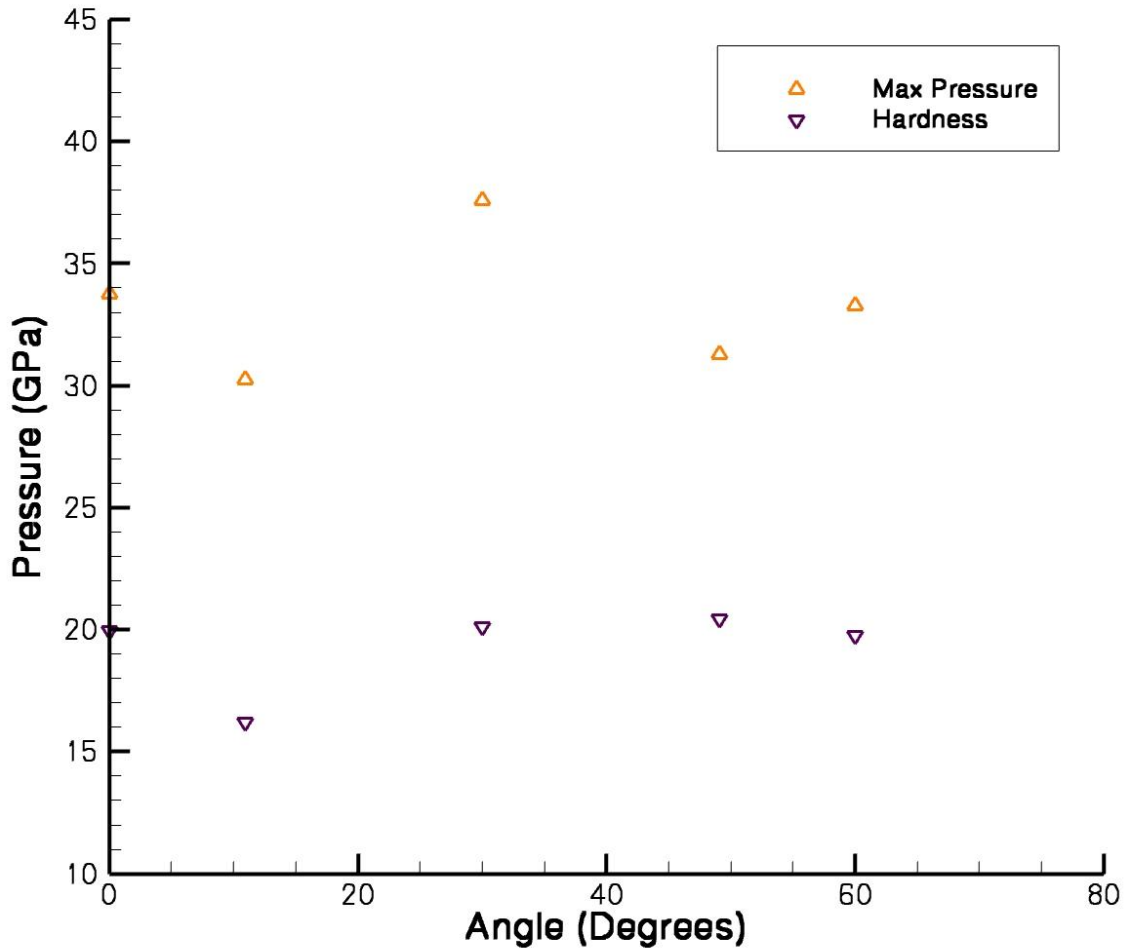


Figure 3.19. Max pressure and hardness for each of the five simulations.

| Angle | Young's Modulus (GPa) | Hardness (GPa) | Max Pressure (GPa) |
|---------|-----------------------|----------------|--------------------|
| 0° | 240.0 | 20.0 | 33.7 |
| 10.893° | 247.6 | 16.2 | 30.2 |
| 30° | 244.2 | 20.1 | 37.6 |
| 49.107° | 248.5 | 20.5 | 31.2 |
| 60° | 239.6 | 19.7 | 33.3 |

Table 3.1. Young's modulus, hardness and max pressure for each of the five models.

CHAPTER 4: INTERPRETATION OF RESULTS

4.1 Inconsistencies in the 30° Model

The 30° model involved nucleation and emission stages which occurred in a short timeframe. This model is notable because the dislocation loop is not absorbed by the free surface, and remains inside the wire. The cause of this is most likely the zero velocity/zero force fixes which were applied to the bottom of the wire. Due to the fact that these atoms were restrained, they were unable to absorb the loop.

The extent to which this affects the wire is unclear. The hardness and max pressure are relatively high for the 30° model. And whether this is an effect of the fixes on the bottom is unknown. A blockage in the path of emitted loops would be a very logical explanation for an increase in pressure.

The bottom boundary is likely to change the force and pressure, after the loop is emitted from the top. However, whether the boundary has an effect before the loop is emitted (i.e. in the elastic regime) is another question. If it does, then perhaps this explains the poor fit of Eq. 2.6 in Figure 3.12.

4.2 Separation of the Nucleation and Emission Stages

Both the 0° and 60° models had loops which nucleated and were emitted while the force and pressure were both decreasing (Figures 3.1, 3.2 and 3.17). The other three models had loops which nucleated during a decrease in force/pressure, then showed an increase in force and pressure, and finally emitted the loops during a second decrease in force and pressure.

All wires can be separated into two groups based on how prismatic loops nucleate and form. These differences manifest themselves in terms of their material properties, which is discussed in Section 4.3.

4.3 Young's Modulus, Max Pressure and Hardness as a Function of Angle

Young's modulus was lowest for the 0° and 60° nanowires. The force-depth curves for these models are also very similar. The wires do not nucleate their first loops (and thus, yield) until further along in the simulations than the other models. The largest Young's modulus values were seen for the 10.893° and 49.107° models. These models also had the earliest nucleation of loops. The 30° model fell right in the middle both in terms of Young's modulus and onset of nucleation. These results show that there is a definite correlation between the Young's modulus and onset of nucleation.

Similar to the Young's modulus, the 10.893° and 49.107° set of models demonstrated max pressure values which were similar. The 0° and 60° models did as well. The maximum pressure was lowest for the 10.893° and 49.107° models. The variation in maximum pressure was significant. Excluding the value for the 30° nanowire, the highest and lowest values differed by 11%.

The trend that hardness showed as a function of angle is difficult to characterize. Most of the wires hovered around a hardness of 20 GPa, except for the 10.893° model. This model had a hardness of

16.2 GPa, which was 23% smaller than the largest value. The 30° model did not seem to be an outlier. However, with the problem with the bottom boundary in that model, there isn't complete confidence in the accuracy of this value.

CHAPTER 5: SUMMARY, CONCLUSIONS & FUTURE WORK

5.1 Summary

Simulations of a 30 nm-diameter, $[1\ 1\ 1]$ -oriented nickel nanowire were performed on five models. The models were all oriented at different axial rotation angles. The simulations showed that as the indenter is applied, force and pressure consistently increase. This results in prismatic dislocation loops to nucleate. After nucleation, the loops will be emitted through the wire. When it gets to the other side of the wire, it will be absorbed by the free surface. For the 30° model, absorption did not occur due to the constraint on the bottom of the wire. The emission process may occur directly after nucleation, or may be delayed. In the case that it is delayed, the pressure and force will increase until emission occurs.

The results of the five simulations show that Young's modulus, maximum pressure and hardness all vary with rotation angle. Young's modulus was determined to be related to the lapse from which prismatic loops are nucleated and emitted. There also appeared to be similarities between the $\{10.893^\circ, 49.107^\circ\}$ and $\{0^\circ, 60^\circ\}$ sets of models based on the force and pressure curves. Similarities also appeared among the $\{10.893^\circ, 49.107^\circ\}$ and $\{0^\circ, 60^\circ\}$ sets. Hardness values were all quite similar except for the 10.893° model, which was much greater than the others.

5.2 Conclusions& Future Work

It is clear that rotational angle plays a role in affecting the dynamics of the indentation process. Unfortunately, the 30° curve, which lies right in the middle of the sampled angles, was subject to error due to the constraint on the bottom of the wire. One way make the model more realistic would be to hold the wire in place with a technique other than altering the forces on the wire. One method would be to place a substrate underneath the wire. Exhaustive attempts were made to create a model like this, with a silicon substrate, but all failed. The potential between nickel and silicon is difficult to model. If this model could be successfully created, the results of these simulations would be more realistic.

Interestingly, there is no consistent trend for each property-angle graph. Although it is somewhat difficult to tell, as we only have confidence in four of the models. More models could easily be created, which would fill in the curves and make the trends more apparent.

If more data was collected, the property-angle curves could be better filled in. It would then be possible to fit a periodic function to each curve. Since the wire is being rotated around its axis, the property-angle graphs should be periodic. It is expected that this curve would be sinusoidal, but the dynamics of dislocation may produce a curve which may not be continuous and/or smooth.

REFERENCES

1. J.J. Mock, S.J. Oldenburg, D.R. Smith, D.A. Schultz, and S. Schultz: Composite plasmon resonant nanowires. *Nano Lett.* **2**, 465 (2002).
2. A. Husain, J. Hone, H.W. Ch. Postma, X.M.H. Huang, T. Drake, M. Barbic, A. Scherer, and M.L. Roukes: Nanowire-based very-high-frequency electromechanical resonator. *Appl. Phys. Lett.* **83**, 1240 (2003).
3. L.A. Bauer, N.S. Birenbaum, and G.J. Meyer: Biological applications of high aspect ratio nanoparticles. *J. Mater. Chem.* **14**, 517 (2004).
4. C.J. Barrelet, A.B. Greytak, and C.M. Lieber: Nanowire photonic circuit elements. *Nano Lett.* **4**, 1981 (2004).
5. Dupont, V. & Sansoz, F. (2009). *Molecular dynamics study of crystal plasticity during nanoindentation in Ni nanowires*.
6. C. Deng and F. Sansoz, "Near-Ideal Strength in Gold Nanowires Achieved through Microstructural Design", *ACS Nano*, **3**, 3001-3008 (2009).
7. C. Deng and F. Sansoz, "Fundamental Differences in the Plasticity of Periodically Twinned Nanowires in Au, Ag, Al, Cu, Pb and Ni", *Acta Materialia*, **57**, 6090-6101 (2009).
8. C. Deng and F. Sansoz, "Enabling Ultrahigh Plastic Flow and Work Hardening in Twinned Gold Nanowires", *Nano Letters*, **9** (4), 1517-1522 (2009).
9. Y. Mishin, D. Farkas, M.J. Mehl, D.A. Papaconstantopoulos, *Phys. Rev. B* **59**, 3393 (1999).
10. G.J. Ackland and A.P. Jones: Applications of local crystal structure measures in experiment and simulation. *Phys. Rev. B: Condens. Matter* **73**, 054104 (2006).
11. G. Feng, W.D. Nix, Y. Yoon, and C.J. Lee: A study of the mechanical properties of nanowires using nanoindentation. *J. Appl. Phys.* **99**, 074303 (2006).
12. K.L. Johnson: *Contact Mechanics* (Cambridge University Press, Cambridge, UK, 1985).
13. M.A. Meyers and K.K. Chawla: *Mechanical Behaviors of Materials* (Prentice Hall, Upper Saddle River, NJ, 1999).

APPENDIX

```

1  echo          both
2  dimension     3
3  boundary      p ff
4  units         metal
5  atom_style    atomic
6  neighbor      2.0 bin
7  neigh_modify  delay 1
8
9  lattice       fcc 3.52
10 region       box block -57.0 57.0 -90.0 37.0 -45.0 45.0
11 create_box    1 box
12
13 #geometry
14 region        wire cylinder x -151.36 0 151.36 INF INF units box
15 region        wireBottom block INF INF INF -299.2 INF INF units box
16
17 mass          1 58.71
18
19 #atoms
20 lattice       fcc 3.52 orient x 1 1 1 orient y 1 1 -2 orient z -1 1 0
21 create_atoms  1 region wire
22
23 #potentials
24 pair_style     eam/alloy
25 pair_coeff     * * ni_mi.fcn Ni
26
27 group         bottomGroup region wireBottom
28 group         mobile subtract all bottomGroup
29
30 timestep      0.005
31 thermo        1000
32
33 compute       1 all ackland/atom
34 compute       2 all ke/atom
35 compute       3 all pe/atom pair
36
37 dump          1 all custom 2500 dump_relax_*.txt x y z id type c_1
38
39 min_style     cg
40 minimize      1.0e-6 1.0e-6 1000 1000
41
42 #initial MD
43 compute       newall temp
44 velocity      all create 300.0 482748 temp new
45
46 #equilibration
47 fix           2 all npt temp 300.0 300.0 0.05 x 0.0 0.0 0.12 couple none drag 2.0
48
49 run           25000
50 unfix        2
51
52 write_restart restart.relax
53
54 undump        1

```

Figure A.1. Code for eam_relax.in for the 0° model. Note that the only Line 20 was changed for simulating the four other models.

```

1  echo                both
2
3  read_restart        restart.relax
4
5  lattice             fcc 3.52
6
7  #potentials
8  pair_style          eam/alloy
9  pair_coeff           ** ni_mi.fcn Ni
10
11 reset_timestep       0
12 compute             newall temp
13 fix                 1 all nvt temp 300.0 300.0 0.05
14 fix                 2 bottomGroup setforce 0.0 0.0 0.0
15 velocity            bottomGroup set 0.0 0.0 0.0
16
17 compute             stress mobile stress/atom
18 fix                 dump mobile ave/spatial 500 10 5000 y center 900. c_stress[2] file force01.dat units box
19
20 timestep            0.005
21 thermo              1000
22 thermo_modify        temp new
23
24 compute             1 all ackland/atom
25
26 dump                1 all custom 2500 dump_centro_*.txt x y z id type c_1
27 restart             50000 calcRstrt
28 variable            y0 equal 91.0
29 variable            vy equal -0.01
30 variable            y equal "v_y0 + step*dt*v_vy"
31 fix                 5 all indent 10. sphere 0.0 v_y 0.0 89.1 units box
32
33 run                 200000

```

Figure A.2. Code for eam_calc01.in for all models.

```

1   echo                both
2
3   read_restart        restart.relax
4
5   lattice             fcc 3.52
6
7   #potentials
8   pair_style          eam/alloy
9   pair_coeff           **ni_mi.fcn Ni
10
11  reset_timestep       0
12  compute              newall temp
13  fix                  1 all nvt temp 300.0 300.0 0.05
14  fix                  2 bottomGroup setforce 0.0 0.0 0.0
15  velocity             bottomGroup set 0.0 0.0 0.0
16
17  compute              stress mobile stress/atom
18  fix                  dump mobile ave/spatial 500 10 5000 y center 900. c_stress[2] file force01.dat units box
19
20  timestep             0.005
21  thermo               1000
22  thermo_modify        temp new
23
24  compute              1 all ackland/atom
25
26  dump                 1 all custom 2500 dump_centro_*.txt x y z id type c_1
27  restart              50000 calcRstrt
28  variable             y0 equal 91.0
29  variable             vy equal -0.01
30  variable             y equal "v_y0 + step*dt*v_vy"
31  fix                  5 all indent 10. sphere 0.0 v_y 0.0 89.1 units box
32
33  run                  200000

```

Figure A.3. Code for eam_calc02.in for all models.

| Angle | Chi-square values for fit of Eq. 2.6 |
|----------------|--------------------------------------|
| 0° | 10,192 |
| 10.893° | 4,890 |
| 30° | 44,371 |
| 49.107° | 4,391 |
| 60° | 8,983 |

Table A.1. Chi-square values from the fit of Eq. 2.6 onto each model's data.